



Article

Fractal Geometry and Convolutional Neural Networks for the Characterization of Thermal Shock Resistances of Ultra-High Temperature Ceramics

Shanxiang Wang¹, Zailiang Chen¹, Fei Qi^{1,*} , Chenghai Xu², Chunju Wang³ , Tao Chen³ and Hao Guo^{3,*} ¹ School of Mechanical and Electric Engineering, Soochow University, Suzhou 215021, China² National Key Laboratory of Science and Technology on Advanced Composites in Special Environments, Harbin Institute of Technology, Harbin 150001, China³ Jiangsu Provincial Key Laboratory of Advanced Robotics & Robotics and Microsystems Center, Soochow University, Suzhou 215021, China

* Correspondence: qifei@suda.edu.cn (F.Q.); hguo@suda.edu.cn (H.G.)

Abstract: The accurate characterization of the surface microstructure of ultra-high temperature ceramics after thermal shocks is of great practical significance for evaluating their thermal resistance properties. In this paper, a fractal reconstruction method for the surface image of Ultra-high temperature ceramics after repeated thermal shocks is proposed. The nonlinearity and spatial distribution characteristics of the oxidized surfaces of ceramics were extracted. A fractal convolutional neural network model based on deep learning was established to realize automatic recognition of the classification of thermal shock cycles of ultra-high temperature ceramics, obtaining a recognition accuracy of 93.74%. It provides a novel quantitative method for evaluating the surface character of ultra-high temperature ceramics, which contributes to understanding the influence of oxidation after thermal shocks.

Keywords: ultra-high temperature ceramics; thermal shock resistance; deep learning; fractal

MSC: 74A40; 74E99; 68T07; 28A80



Citation: Wang, S.; Chen, Z.; Qi, F.; Xu, C.; Wang, C.; Chen, T.; Guo, H. Fractal Geometry and Convolutional Neural Networks for the Characterization of Thermal Shock Resistances of Ultra-High Temperature Ceramics. *Fractal Fract.* **2022**, *6*, 605. <https://doi.org/10.3390/fractalfract6100605>

Academic Editors: Branislav Randjelovic, Cristina Serpa and Hans-Jörg Fecht

Received: 2 August 2022

Accepted: 6 October 2022

Published: 17 October 2022

Publisher's Note: MDPI stays neutral with regard to jurisdictional claims in published maps and institutional affiliations.



Copyright: © 2022 by the authors. Licensee MDPI, Basel, Switzerland. This article is an open access article distributed under the terms and conditions of the Creative Commons Attribution (CC BY) license (<https://creativecommons.org/licenses/by/4.0/>).

1. Introduction

Ultra-high temperature ceramics (UHTCs) are an emerging class of materials that can keep their physical and chemical structure stable under high temperatures. These materials include refractory borides, carbides, and transition metal nitrides, such as ZrB_2 , TaC, etc. [1,2]. With the rapid development of UHTCs used in aviation, nuclear energy, military equipment, and the automobile industry, this class of materials has attracted much attention for employment in extreme environments [3]. ZrB_2 , for example, has been shown to have high antioxidant properties [4,5]. In ZrB_2 composites, SiC is usually introduced as the second phase to inhibit grain growth and improve sintering performance, oxidation performance, and mechanical properties [6,7]. The effects of the microstructure on ceramic properties have been reported in many relevant fields. Chu et al. [8] analyzed γ -dicalcium silicate-based low-carbon materials and discussed the roles of particle packing and water-coating thickness in the carbonation and strength of this material. However, due to the inherent brittleness of UHTCs, they are prone to catastrophic damage when subject to high temperature differences under rapid heating or cooling. Evaluating the thermal shock resistance and fracture strength of UHTCs at high temperatures is an essential problem [9].

The thermal shock failure criteria and thermal shock resistance characterization model have been established for this kind of material, and researchers are currently striving to accurately evaluate their thermal shock resistance [9]. Along with investigations into the optimal design [10] and the heterogeneous materials introduced [11], the description

of the complexity of the structures has become a salient problem. The utilization of the microstructure of UHTCs to reveal the damage to the materials following thermal shocks has become a commonly used method, comparing and extracting features such as the oxidized surface [2], fracture surface [12], crack propagation path [13], and fretting wear scars [14]. However, it is inconvenient and difficult to extract the material damage features when the material structure is complex. Therefore, a quantitative approach to extract damage features from complex microstructures, which would be beneficial for the evaluation of the damage to mechanical properties, is urgently needed.

Daghighi et al. [15] applied machine learning to excavate the internal relationship between different particle fillers and the fracture toughness of particle-reinforced composites. Konstantopoulos et al. [16] used a machine learning classification model to process nanoindentation data and identify interface reinforcement. In traditional machine vision-based image recognition, experts manage and define feature information and design and provide corresponding feature extraction and classification algorithms, which have good recognition characteristics. However, the robustness of different features and the efficiency of recognition still require significant work.

In the prediction of mechanical properties of composite materials, a large amount of data is obtained based on experimental tests and numerical simulation. Combined with artificial intelligence, researchers can establish rapid responses between parameters and properties. Laban et al. [17] used artificial neural networks to predict the quasi-static compressive bearing capacity of composite circular tubes subjected to low-speed impact loads through the initial peak force, average load, and crushing force efficiency and successfully modeled the highly nonlinear behavior with a mean square error of 0.191 N. Artero-Guerrero et al. [18] predicted the ballistic limit of a composite under different layering orders based on an artificial neural network. The errors in the artificial neural network prediction results for the training set and test set were 3.7% and 7%, respectively. It was concluded that laying 0° and 90° laminates on the impact side of the composite material was helpful in improving the ballistic limit of the composite laminates and could guide the design of composite materials. Using neural networks, Yan et al. [19] proposed an efficient multiscale framework for composite substitution modeling considering progressive damage behavior.

With the development of deep learning models, automatic extraction of material damage features for the identification of damage types has demonstrated advantages such as high efficiency and low cost [20]. Such methods can help in extracting and describing complex image features and significantly reduce the required labor [21]. Yang et al. [22] predicted complex stress and strain fields in layered composites using deep learning. The convolutional neural network (CNN) model has powerful feature extraction, nonlinear mapping, and generalization capabilities [23]. Yu et al. [24] applied an AI-based approach in the optimal design of 2D nanocomposites, identifying high-performance solutions with maximum toughness or strength. A CNN model was used to obtain the toughness or strength, and a global optimizer was used to search the design space of the 2D nanocomposite graphene.

Although CNN models have powerful image feature recognition abilities, irregular and inhomogeneous microstructures can make feature recognition difficult. The fractal method, as a nonlinear mathematical method, can be used to effectively evaluate the irregularity and complexity of geometrical morphologies. Roberto et al. [25] predicted and classified histological images through fractal recombination features.

The surfaces of UHTCs in extreme environments are oxidized after thermal shocks. The oxidation structures influence the residual strength of UHTCs following thermal shocks [26]. This paper provides a fractal feature recombination method for the oxidized surfaces of UHTCs following thermal shocks. Then, a convolution neural network model based on the fractal recombination image is established. The relationship between the microstructure of the oxidized surface and the strength of UHTCs is discussed. Furthermore, a fusion

model combining the oxidized surface image and the fractal feature reconstruction image is established and verified.

2. Methodology

2.1. Thermal Shock Experiment

In this study, the properties of ZrB_2 -20%vol.SiC composites following repeated thermal shocks were investigated. ZrB_2 -SiC ceramics were prepared through hot pressing for 1 h at 1900 °C and 30 MPa under a uniaxial load. The prepared ZrB_2 -SiC ceramic material was cut, with its tensile surface perpendicular to the direction of hot pressing. The sample size was 36 mm × 4 mm × 3 mm, following the GB/T 6569-2006/ISO 14704: 2000 standard. The samples were subjected to thermal shock treatment with electric heating equipment. Six samples were tested under different thermal shock conditions. The temperatures of the samples' centers were measured using thermocouples and a double specific-heat infrared thermometer. When the temperature reached 1600 °C, the system circuit was closed and a thermal shock was recorded. Thermal shocks with 10, 20, 30, and 50 cycles were used. The heating rate was 80 °C/s. The residual strength after the thermal shocks was measured with a three-point bending test. The microstructures of the oxidized surface were observed with a scanning electron microscope (SEM), as shown in Figure 1. Experimental details can be found in our previous studies [26]. From the microstructures, it can be seen that the images of the oxidized surfaces were complex, and they were difficult to describe using regular geometries.

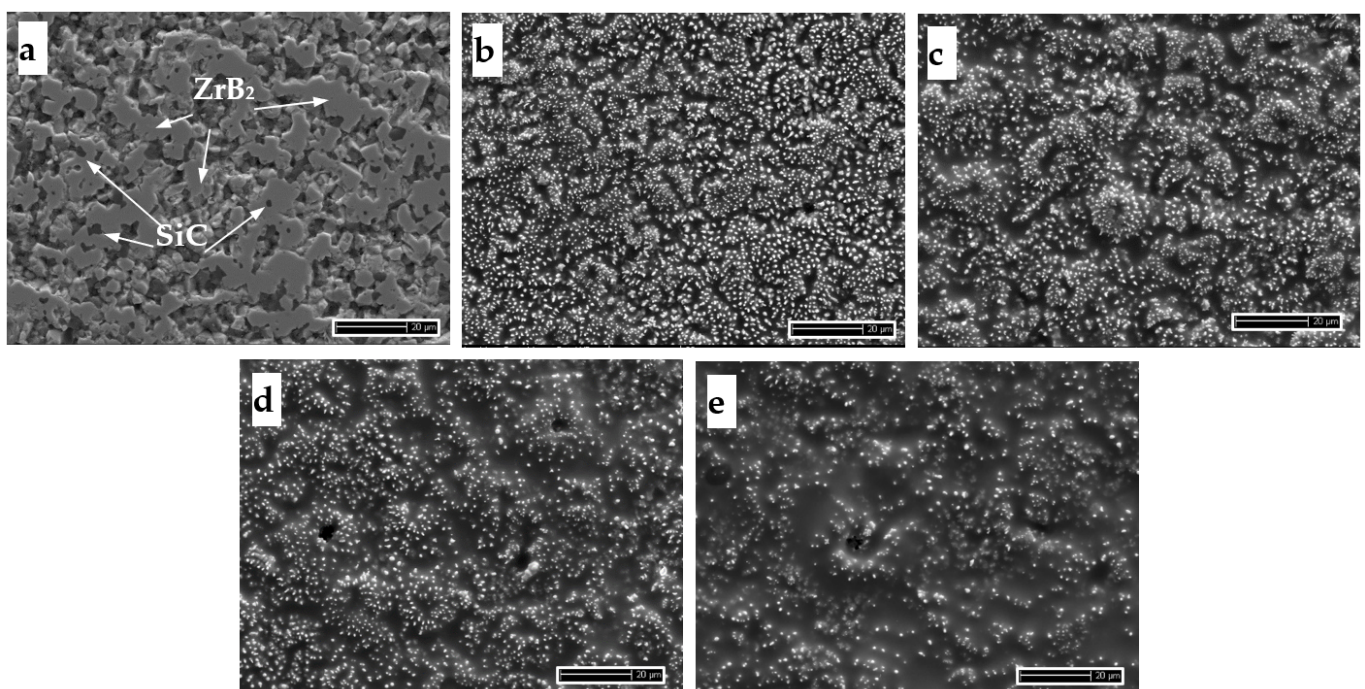


Figure 1. Micrographs of the original specimen (a) and the specimens shocked with 10 (b), 20 (c), 30 (d), and 50 (e) cycles. The scale of the images is 20 μm . In (a), ZrB_2 is gray and the SiC is a dark color in the composites.

2.2. Fractal Feature Recombination Method

Fractal geometry is a field that deals with geometrical structures that cannot be defined using Euclidean geometry. In computer vision, the most prominent algorithms are the box-counting [27] and gliding-box [28] algorithms. The application of these algorithms consists in splitting the images onto different scales and then extracting features from each sub-image. For the representation of numerical features using fractal approaches, we used the fractal dimension (FD), lacunarity (LAC), and percolation (PERC), which were judged

to be three of the most relevant approaches. A multiscale and multidimensional analysis of the images was performed to obtain these features. The gliding-box [28] algorithm, which can be applied to process images of different resolutions and sizes, was employed as a multidimensional analysis method.

Three color distance measures—namely, the chessboard (Δ_h), Minkowski (Δ_n), and Manhattan (Δ_m) distances—were employed, as shown in Equations (1)–(3) [28]:

$$\Delta_h = \max(|f_i(k_i) - f_c(k_c)|), k \in r, g, b \tag{1}$$

$$\Delta_n = \sqrt[p]{\sum_k ((f_i(k_i) - f_c(k_c))^p), k \in r, g, b} \tag{2}$$

$$\Delta_m = \sum_k |f_i(k_i) - f_c(k_c)|, k \in r, g, b \tag{3}$$

When box β was moved, a multidimensional analysis of the color similarity was performed for each pixel in the box. The center vector $f_c = (r_c, g_c, b_c)$ represents the color intensity of the three-color RGB channels. Other pixels in the border are also assigned $f_i = (r_i, g_i, b_i)$.

The FD, LAC, and PERC are described by five functions: $C(L)$, $Q(L)$, $M(L)$, $\Lambda(L)$, and $D(L)$ [25]. From the five characteristic functions of the FD, LAC, and PERC, 300 fractal features were obtained. The details can be found in Appendix A. Then, these features were reshaped into $10 \times 10 \times 3$ RGB images, and the process is shown in Figure 2.

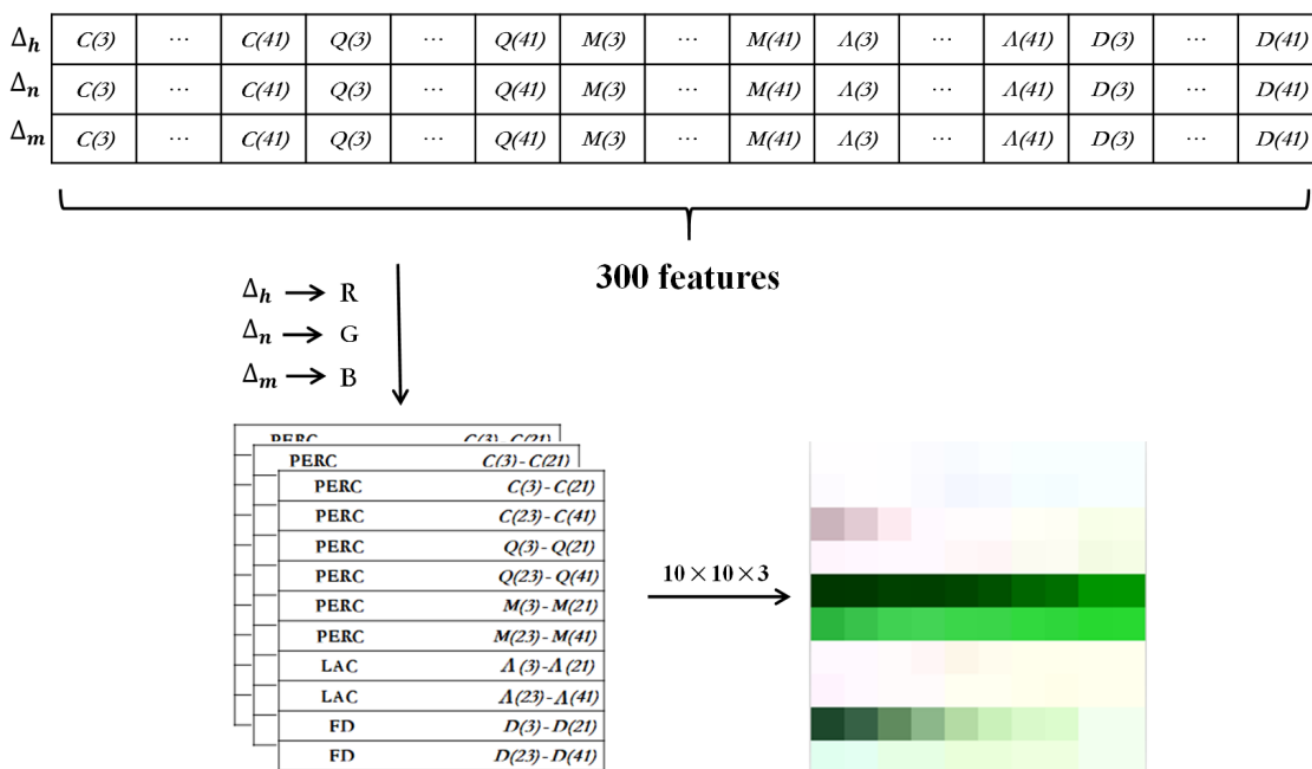


Figure 2. In the process of fractal feature recombination, 300 features were obtained from the five functions of the FD, LAC, and PERC, and these features were reconstructed into $10 \times 10 \times 3$ RGB images.

However, the Minkowski distance also changes due to different p values. The Minkowski distance is an extension of the Euclidean distance. When p is 2, it results in a Euclidean distance. With changing values of p , 100 different features could be obtained. We randomly selected one image from each category. It showed that the standard deviation of the feature reached the maximum when p equaled 3. This also indicated that the range of the features was the largest, as shown in Figure 3.

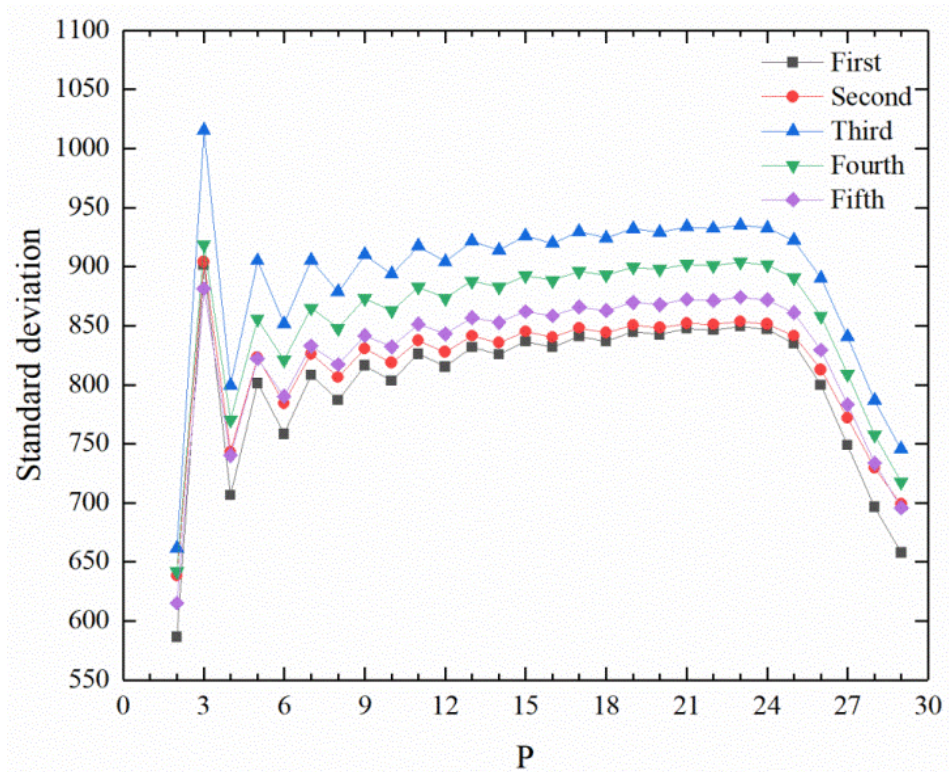


Figure 3. Using the Minkowski distance, the standard deviation of the features was obtained with different p values.

Based on the Minkowski distance, 100 features could be extracted from the image and recombined into a 10×10 matrix. In Figure 4, the gray co-occurrence matrix (GLCM) obtained by processing the reconstructed matrix is shown. Four different angle-scanning directions of 0° , 45° , 90° , and 135° were selected, and offset d was set as 1. Then, the matrix was processed to obtain four different GLCMs. Finally, the energy was extracted from the GLCM using Equation (4) [29]. As shown in Figure 5, when p was 3, the average energy was the largest relative to other p values. This also indicated that, when $p = 3$, the elements in the GLCM were most concentrated. To sum up, $p = 3$ was the most appropriate for the Minkowski distance.

$$Energy = \sum_{i,j=0}^{N-1} P_{(d,\theta)}(i,j)^2 \tag{4}$$

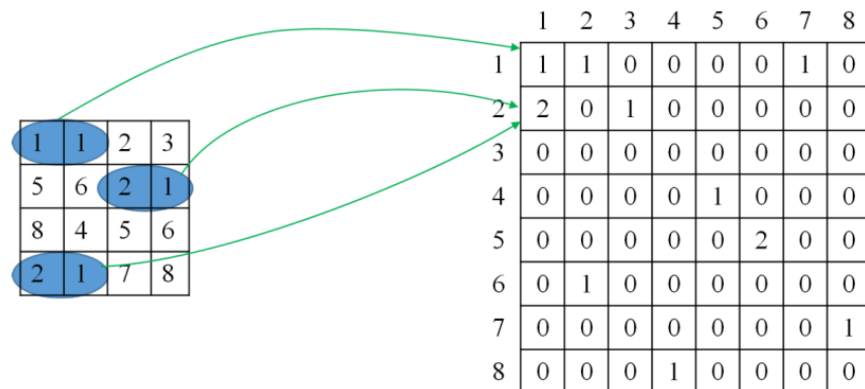


Figure 4. Example of a gray level co-occurrence matrix.

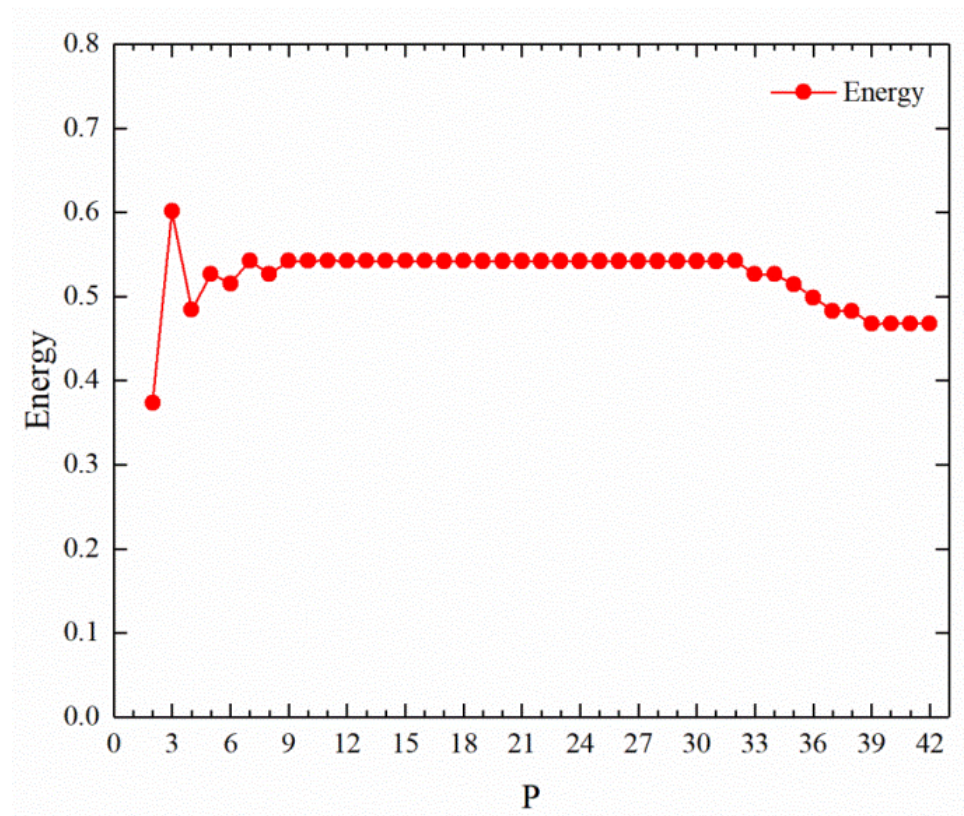


Figure 5. The gray level co-occurrence matrix was calculated to obtain the average value of the energy with different values of p .

2.3. Model Selection

ResNet, which introduced the residual learning framework of deep feedforward neural networks, was first proposed by He et al. [30]. In recent years, ResNet and its variants have achieved excellent performance and become the dominant models in image processing. They have been integrated into current popular processing models, such as the region-based convolutional neural network (RCNN) [31]. ResNet [32] has been widely used in various feature extraction applications. However, when a CNN reaches a certain depth, further deepening of the classification effect does not lead to improvements but to slower network convergence speed and lower accuracy. Even if the dataset is enlarged and the over-fitting problem is solved, the classification performance and accuracy will not be improved. The emergence of the residual network can solve this problem to a certain extent. Thus, we used the ResNet-50 model in this article.

2.4. Model Fusion

Firstly, the sliding-box algorithm was used to place a square box with pixel $L \times L$ in the upper left corner of the image, and the box was slid continuously to the right, one row at a time, and down one row to the right of the image. When the end of the image was reached, the box was repositioned at the starting point and the L value increased by 2. The initial value of L was set to 3 and the maximum value was 41. Then, feature extraction of the FD, LAC, and PERC for these boxes was used to obtain a total of 100 features from the five functions $C(L)$, $Q(L)$, $M(L)$, $\Lambda(L)$, and $D(L)$. By selecting three different distances, 300 features could be obtained. Finally, the 300 features were reconstructed into a $10 \times 10 \times 3$ artificial color image.

The training set of the original images was input into the CNN model, and the optimal model O-Resnet was obtained by continually adjusting the learning rate, batch size, epoch, and dropout. Similarly, the reconstructed images of the fractal features were input into the CNN model, and the optimal model F-ResNet was obtained after the corresponding

adjustment. Based on the test set, the original image and the fractal reconstruction image were input into O-ResNet and F-ResNet, respectively, and the classification and recognition results were output, respectively. Then, the quasi-probability values of the two models were added according to the sum rule, finally, the model fusion result and the predicted class were obtained. The overall process is shown in Figure 6.

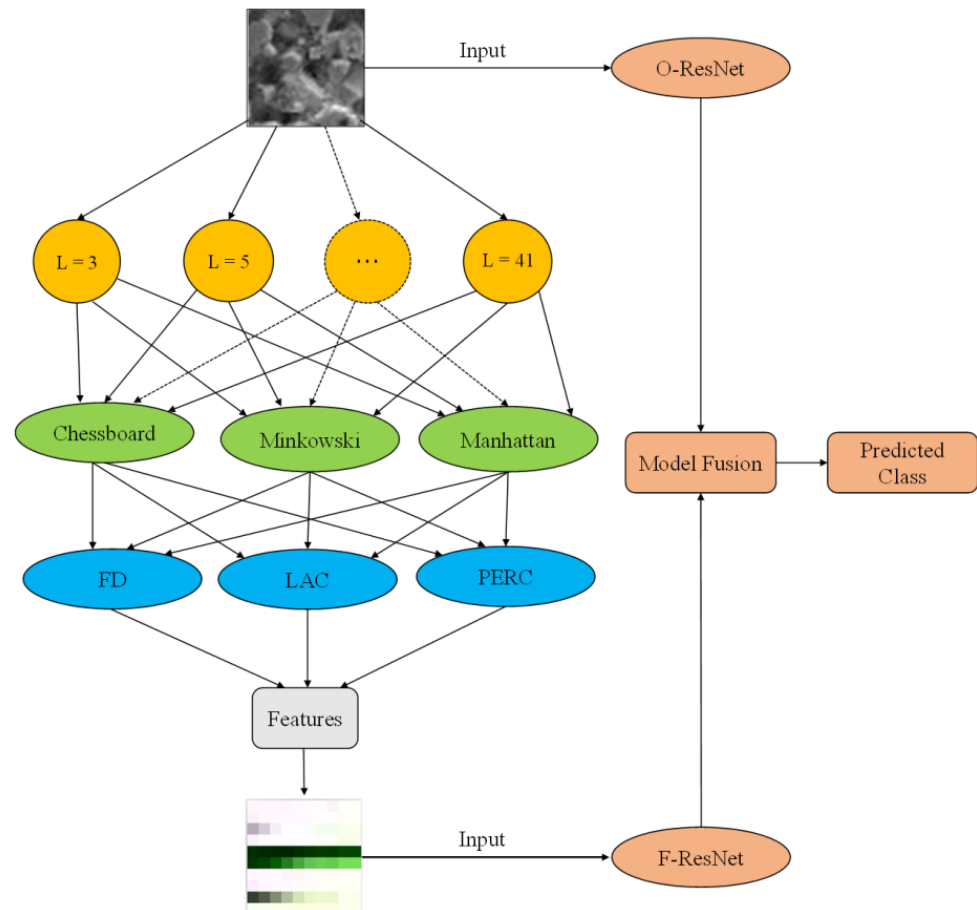


Figure 6. The process of image feature extraction and classification for the oxidized surface after thermal shocks, including the O-ResNet model, F-ResNet model, and fusion model.

3. Experimental Results and Analysis

3.1. Dataset

3.1.1. Microscopic Image Acquisition of Oxidized Surface

The original dataset in this study consisted of 10 SEM images of a ZrB_2 -SiC oxidized surface following repeated thermal shocks. There were five categories; namely, those for 0, 10, 20, 30, and 50 thermal shock cycles. Zero corresponded to the surface morphology without thermal shocks. The image resolution was 500 dpi and the pixel size was 645×478 . The number of thermal shocks cycle provided the classification of the corresponding target.

3.1.2. Data Preprocessing

To ensure the reliability of the model and improve the training accuracy, the dataset of the image was enhanced. We first clipped the images of the original dataset; that is, set a sliding window with a size of 50×50 for each image. Every time the sliding window moved to a new position, we made a judgment based on its position. If the window did not exceed the right or bottom boundary of the original image, we cropped its position. Otherwise, we did not cut it and moved directly to the next position. In this study, the window sliding step was set to 35 and, finally, each original picture was cropped into 234 images with pixels of 50×50 . To further expand the dataset, random rotation, trans-

lation, scaling, flipping, and shearing were used. Then, the extended dataset was reconstructed with fractal features, as shown in Figure 7. The oxidized surface images of ZrB₂-SiC ceramics with different numbers of thermal shock cycles (0, 10, 20, 30, and 50) were divided into five categories: first, second, third, fourth, and fifth. Based on the fractal feature extraction method described in Section 2.4, the fractal features extracted from each category of images were reconstituted into chromaticity maps. Finally, the reconstructed images of the fractal features were input into the deep learning model.

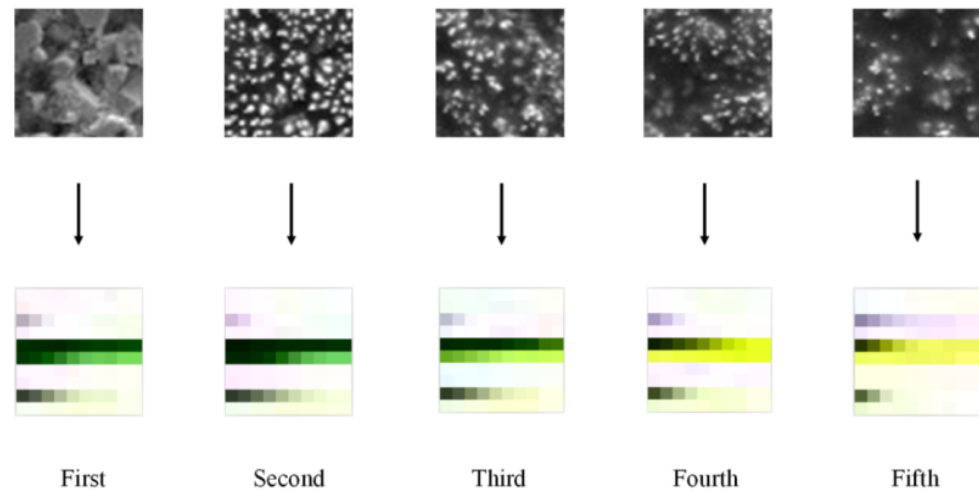


Figure 7. Fractal feature images were reconstructed from oxidized surface clipping images of ZrB₂-SiC under different numbers of thermal shock cycles.

3.2. Experimental Parameter Settings and Evaluation Indicators

3.2.1. Parameter Settings

The dataset from the expanded original image and fractal feature reconstruction image was divided into the training set, validation set, and test set in the ratio of 6:2:2, respectively. At the same time, the image from the dataset was resized to $3 \times 224 \times 224$ as the input of the model. In the process of model training, the initial learning rate for training the two ResNet models was 0.005, the learning rate drop factor was 0.001, the batch size was 128, the number of iterations was 20, and the cross-entropy loss function was used. Generalized regularization was added to the training models to prevent over-fitting of the training system. Finally, the softmax classifier was used to output the final identification results and a random gradient descent method to learn parameters.

3.2.2. Experimental Evaluation Index

In multi-target detection and classification, accuracy is the most important evaluation index; that is, the percentage of the quantity correctly predicted by the model compared to the total quantity. This study compared the accuracy of each model as the evaluation standard. In addition to accuracy, the evaluation criteria for the models included precision and recall. Precision is the proportion of the sample identified as positive that is actually positive. The recall rate is the proportion of positive samples correctly identified as positive. The calculation formulas for each evaluation index are shown in Equations (5)–(7):

$$Acc = \frac{TP + TN}{TP + FN + FP + TN} \quad (5)$$

$$Pre = \frac{TP}{TP + FP} \quad (6)$$

$$Recall = \frac{TP}{TP + FN} \quad (7)$$

TP refers to the number of positive classes correctly predicted as positive. *TN* is the number of negative classes correctly predicted as negative. *FP* is the number of negative classes incorrectly predicted as positive. *FN* is the number of positive classes wrongly predicted as negative.

The statistics in Table 1 are the results of O-ResNet for the above algorithm indicators. The statistics in Table 2 are the results of F-ResNet. Table 3 shows the fusion results of the O-ResNet and F-ResNet models. Figure 8a–c display the variation tendencies for the accuracy, precision, and recall statistics shown in Table 1, Table 2, and Table 3, respectively.

Table 1. The classification results for O-ResNet.

Category	Accuracy (%)	Precision (%)	Recall (%)
First	100.0	100.0	100.0
Second	100.0	100.0	100.0
Third	91.5	84.2	71.6
Fourth	90.1	73.6	79.1
Fifth	98.1	93.0	98.5

Table 2. The classification results for F-ResNet.

Category	Accuracy (%)	Precision (%)	Recall (%)
First	90.5	81.3	77.6
Second	97.4	90.5	100.0
Third	83.9	61.4	66.2
Fourth	81.9	58.3	52.2
Fifth	94.1	89.2	86.6

Table 3. The classification results for O-F-ResNet (Fusion model).

Category	Accuracy (%)	Precision (%)	Recall (%)
First	100.0	100.0	100.0
Second	100.0	100.0	100.0
Third	93.0	85.5	79.1
Fourth	91.3	77.9	79.1
Fifth	98.1	93.0	98.5

3.3. Result Analysis

As shown in Tables 1–3, the average accuracy of the fusion model O-F-ResNet was improved by 0.54% compared to O-ResNet and by 6.52% compared to F-ResNet. O-F-ResNet was 1.12% more accurate on average than O-ResNet and 15.14% more accurate than F-ResNet. The average recall rate of O-F-ResNet was 1.50% higher than that of O-ResNet and 14.82% higher than that of F-ResNet. The fusion model had the highest average accuracy. The fractal features increased the recognition accuracy in the fusion model, especially for the third and the fourth categories, as shown in Figure 8.

As can be seen from Table 4, the residual strength increased after repeated thermal shocks. The formation of a silica-rich scale is considered to improve oxidation resistance, and such scales are effective in certain temperature, pressure, and external gas velocity regimes [3]. When the number of thermal shock cycles was increased to 20, the bending strength continued to increase. However, when the number of thermal shock cycles reached 30, the bending strength of the sample was smaller than that after 10 and 20 thermal shock cycles. The reason is that, with the increase in thermal shock cycles, more gas products were produced by the oxidation of the sample. For example, gaseous products, such as CO and B₂O₃, leave many holes when they pass through the oxide layer, which can possibly reduce ceramic strength. However, when the number of thermal shocks rose to 50 cycles, the pores in the oxide layer did not show an obvious increasing trend and the silica-rich glass phase was denser than before, which led to a higher strength than 30 cycles.

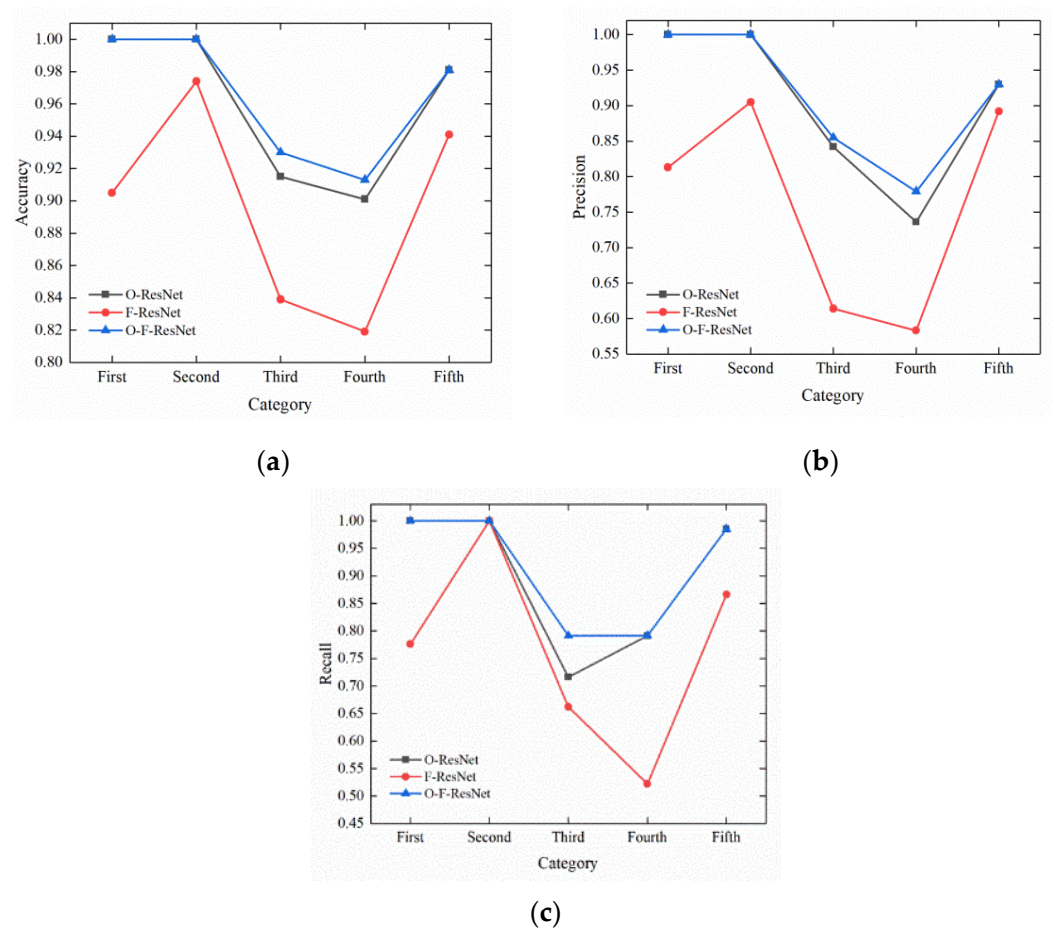


Figure 8. The accuracy (a), precision (b), and recall (c) of classification prediction with different models.

Table 4. Relationships between thermal shock cycles and residual strength [26].

Thermal Shock Cycles	Bending Strength (MPa)
0	440 ± 47
10	514 ± 34
20	645 ± 60
30	494 ± 147
50	589 ± 72

In this study, fractal geometry features combined with convolutional neural networks were used to investigate thermal shock cycles applied to UHTCs. Quantitatively extracting features of the surface microstructure of UHTCs after thermal shocks can contribute to evaluating their thermal shock resistance. This method can be expanded to recognize the damage features of composites. Using microstructures of materials to distinguish their loading conditions can help to provide early warnings before the material fractures.

4. Conclusions

In this paper, a characterization method for the oxidized surface of ultra-high temperature ceramics was proposed, and a correlation model for the oxidized surface microstructures and thermal shock properties of materials based on fractal features and deep learning was constructed. The main conclusions are as follows:

- (1) A fractal feature recombination method for the oxidized surface of ultra-high temperature ceramics after thermal shocks was described. It is a novel method for the extraction of irregular and inhomogeneous microstructures of oxidized surfaces. The method transformed the parameters of fractal features into chromaticity maps suitable

to input into deep learning models. In the image feature extraction process, the gray co-occurrence matrix was obtained by processing the reconstructed matrix. The p value was calculated and $p = 3$ resulted in the appropriate Minkowski distance for our images;

- (2) The original images and the recombination images of the fractal features with different numbers of thermal shock cycles were respectively input into the deep learning model and the model was fused in the softmax layer. Ultimately, the classification accuracy of the oxidized surface image reached 93.47%. It was verified that the fusion model could effectively identify the categories of oxidized surface images under different thermal shock cycles. The fractal features were able to increase the recognition accuracy in the fusion model;
- (3) A quantization method for the oxidized surface of ultra-high temperature ceramics with different numbers of thermal shock cycles was described. The relationship between the oxidized surface of the material and the strength was discussed.

In the future, distance calculation formulas other than the chessboard, Minkowski, and Manhattan distances could be selected to obtain fractal features, and different feature arrangement methods could be employed to further improve image classification performance. In the process of composite structure assembly and use, our method can also be used to detect the damage to composites, which can help to improve the reliability of structures.

Author Contributions: Conceptualization, H.G. and F.Q.; methodology, S.W.; validation, Z.C. and F.Q.; Resources, C.X.; supervision, C.W.; writing—original draft preparation, S.W.; writing—review and editing, H.G., S.W. and F.Q.; funding acquisition, H.G., F.Q. and T.C. All authors have read and agreed to the published version of the manuscript.

Funding: This work was supported by the Science Foundation of the National Key Laboratory of Science and Technology on Advanced Composites in Special Environments (grant no. JCKYS2020603C017), the National Natural Science Foundation of China (grant nos 11402156, 61503269, and 62073229), and the National Key Research and Development Program of China (grant no. 2019YFB1310900).

Institutional Review Board Statement: Not applicable.

Informed Consent Statement: Not applicable.

Data Availability Statement: Not applicable.

Conflicts of Interest: The authors declare no conflict of interest.

Appendix A. Fractal Feature Extraction Process

In this study, fractal-based methods were used to represent structures through observations at different scales. The most prominent algorithms for this purpose are the box-counting [27] and gliding-box [28] algorithms. These algorithms involve splitting images into different scales and then extracting features from each sub-image. For the representation of numerical features using fractal approaches, the fractal dimension (FD), lacunarity (LAC), and percolation (PERC) are three of the most relevant features [25]. A multiscale and multidimensional analysis of the image was performed in order to obtain these features. The multidimensional analysis method we chose was the gliding-box [28] algorithm. This algorithm consists of placing a box β sized $L \times L$ in the upper-left corner of the image, where L is given in pixels. This box glides through the image, one column and then one row at a time. After reaching the end of the image, the box is repositioned at the starting point and the value of L is increased by 2. In an image sized $H \times W$, the total number T of boxes for a scale L is given by Equation (A1):

$$T(L) = (H - L + 1) \times (W - L + 1) | L \leq (H, W) \quad (\text{A1})$$

When box β is moved, a multidimensional analysis of color similarity is performed for each pixel in the box. The center vector $f_c = (r_c, g_c, b_c)$, represents the color intensity of

the three-color RGB channels. Other pixels in the border are also assigned $f_i = (r_i, g_i, b_i)$. Then, the box is binarized by calculating the color distance between f_c and f_i to determine the size. As shown in Equations (A2)–(A4) [28], three color distance measures—namely, the chessboard (Δ_h), Minkowski (Δ_n), and Manhattan (Δ_m) distances—were chosen:

$$\Delta_h = \max(|f_i(k_i) - f_c(k_c)|), k \in r, g, b \tag{A2}$$

$$\Delta_n = \sqrt[3]{\sum_k ((f_i(k_i) - f_c(k_c))^3), k \in r, g, b} \tag{A3}$$

$$\Delta_m = \sum_k |f_i(k_i) - f_c(k_c)|, k \in r, g, b \tag{A4}$$

f_i is marked as 1 if the calculated distance between f_c and f_i is less than or equal to the box's border L ; otherwise, f_i is marked as 0. Figure A1 shows a schematic diagram of the calculation of the color distance for a box with a 3×3 border.

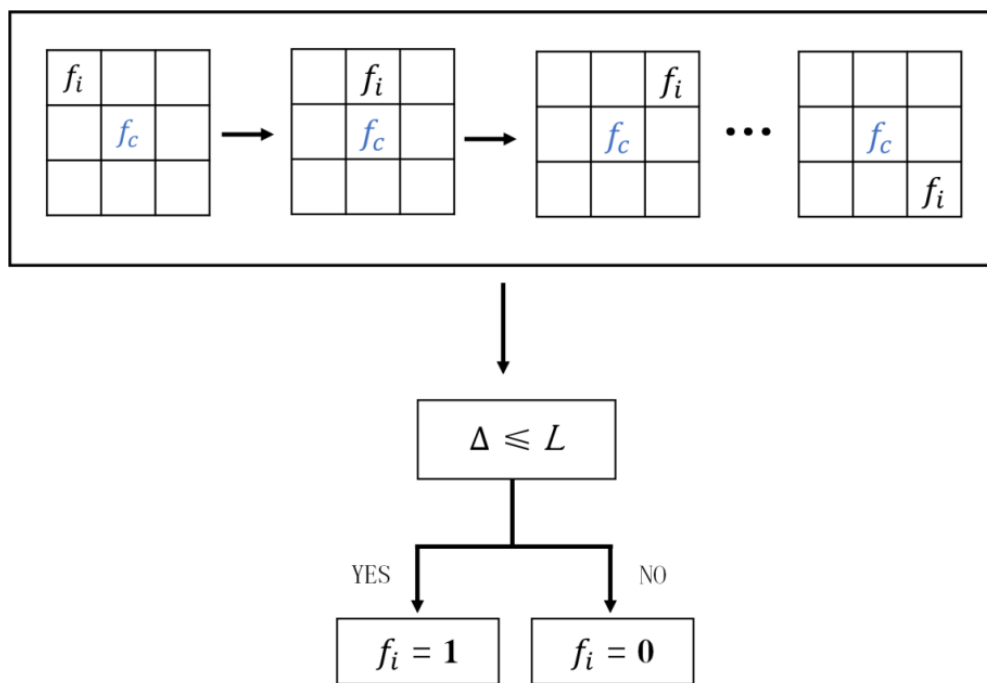


Figure A1. Binarization diagram.

The aim of the process is to convert a box containing RGB into a box containing binary. After the binarization of each box with frame L , the corresponding structure of the probability matrix is generated, and each element in the matrix corresponds to probability P .

Taking a 3×3 box as an example, the image with a box with a border $L = 3$ is traversed. After binarization, we get a total of N boxes. The number of pixels marked 1 in each box is then counted. A box with only 1 pixel equal to 1 is labeled $n(1, 3)$. A box with only 2 pixels equal to 1 is labeled $n(2, 3)$. By analogy, a box with only 1 pixel equal to 1 is labeled $N(9, 3)$. At this point, $n(1, 3) + n(2, 3) + \dots + n(9, 3) = N$, and let $P(m, 3) = n(m, 3)/N$.

The FD is the feature most commonly used to evaluate the fractal characteristics of images and involves the irregularity and complexity of fractals. To obtain the eigenvalues of the local FD from the probability matrix for each value of scale L , Equation (A5) can be used [28]:

$$D(L) = \sum_{m=1}^{L^2} \frac{P(m, L)}{m} \tag{A5}$$

The LAC is a complement to the FD and can further be used to evaluate the distribution and filling of fractal space. Based on the probability matrix, the first-order

matrix in Equation (A6) and the second-order matrix in Equation (A7) can be calculated as follows [28]:

$$\mu(L) = \sum_{m=1}^{L^2} mP(m, L) \tag{A6}$$

$$\mu^2(L) = \sum_{m=1}^{L^2} m^2P(m, L) \tag{A7}$$

The LAC value with the border L is given by $\Lambda(L)$, as shown in Equation (8):

$$\Lambda(L) = \frac{\mu^2(L) - (\mu(L))^2}{(\mu(L))^2} \tag{A8}$$

The PERC is a physical phenomenon that mainly involves the properties of a fluid in porous media. This concept can be used to verify some of the cluster properties of image pixel neighborhoods. After the color distance Δ is calculated, the binary matrix generated is marked by a clustering marking algorithm; that is, the nearby pixel group meeting the Δ distance criterion is marked, as shown in Figure A2.

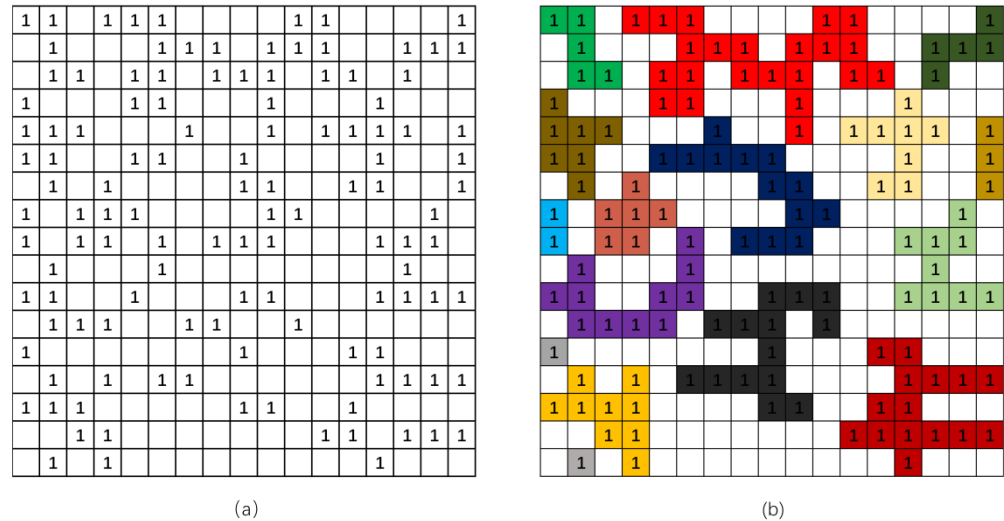


Figure A2. (a) Binary matrix and (b) cluster-labeled matrix.

Assume that c_i is the number of clusters in box β and represents the characteristics of the average number of clusters in each box with side length L . As shown in Equation (A9), this is given by the feature $C(L)$ [28]:

$$C(L) = \frac{\sum_{i=1}^{T(L)} c_i}{T(L)} \tag{A9}$$

It is assumed that m_i is the size of the maximum number of clusters in box β . The average coverage area of the largest clusters in each box with side length L is given by the feature $M(L)$ [28], as shown in Equation (A10):

$$M(L) = \frac{\sum_{i=1}^{T(L)} \frac{m_i}{L^2}}{T(L)} \tag{A10}$$

We can also verify that box β is permeable by specifying permeable thresholds for different types of structures. In this matrix, the threshold is set to $p = 0.59275$. If the ratio of the number of pixels marked 1 to the total number of pixels in the matrix is greater than or equal to p , the matrix is considered permeable. By setting Ω_i to the number of pixels

marked 1 in box β with size $L \times L$, we can determine whether the box is infiltrating with Equation (A11):

$$q_i \begin{cases} 1, & \frac{\Omega_i}{L^2} \geq 0.59275 \\ 0, & \frac{\Omega_i}{L^2} < 0.59275 \end{cases} \quad (\text{A11})$$

Then, we can obtain the binary value of q_i , where 1 indicates that the box is infiltrating. Feature $Q(L)$ represents the average number of seepage occurrences in the box with side length L , which can be obtained from Equation (A12) [28]:

$$Q(L) = \frac{\sum_{i=1}^{T(L)} q_i}{T(L)} \quad (\text{A12})$$

From the above five characteristic functions of FD, LAC, and PERC, 300 fractal features can be obtained.

References

- Jin, X.; Fan, X.; Lu, C.; Wang, T. Advances in oxidation and ablation resistance of high and ultra-high temperature ceramics modified or coated carbon/carbon composites. *J. Eur. Ceram. Soc.* **2018**, *38*, 1–28. [\[CrossRef\]](#)
- Opeka, M.M.; Talmy, I.G.; Wuchina, E.J.; Zaykoski, J.A.; Causey, S.J. Mechanical, thermal, and oxidation properties of refractory hafnium and zirconium compounds. *J. Euro. Ceram. Soc.* **1999**, *19*, 2405–2414. [\[CrossRef\]](#)
- Fahrenholtz, W.G.; Hilmas, G.E. Ultra-high temperature ceramics: Materials for extreme environments. *Scr. Mater.* **2017**, *129*, 94–99. [\[CrossRef\]](#)
- Zhang, G.J.; Ni, D.W.; Zou, J.; Liu, H.T.; Wu, W.W.; Liu, J.X.; Suzuki, T.S.; Sakka, S. Inherent anisotropy in transition metal diborides and microstructure/property tailoring in ultra-high temperature ceramics—A review. *J. Eur. Ceram. Soc.* **2018**, *38*, 371–389. [\[CrossRef\]](#)
- Chaim, R.; Chevallier, G.; Weibel, A.; Estournes, C. Grain growth during spark plasma and flash sintering of ceramic nanoparticles: A review. *J. Mater. Sci.* **2018**, *53*, 3087–3105. [\[CrossRef\]](#)
- Gui, K.; Liu, F.; Wang, G.; Huang, Z.; Hu, P. Microstructural evolution and performance of carbon fiber-toughened ZrB_2 ceramics with SiC or ZrSi_2 additive. *J. Adv. Ceram.* **2018**, *7*, 343–351. [\[CrossRef\]](#)
- Yan, X.; Jin, X.; Li, P.; Hou, C.; Hao, X.; Li, Z.; Fan, X. Microstructures and mechanical properties of ZrB_2 -SiC-Ni ceramic composites prepared by spark plasma sintering. *Ceram. Int.* **2019**, *45*, 16707–16712. [\[CrossRef\]](#)
- Chu, S.H.; Chen, J.J.; Li, L.G.; Ng, P.L.; Kwan, A.K.H. Roles of packing density and slurry film thickness in synergistic effects of metakaolin and silica fume. *Powder Technol.* **2021**, *387*, 575–583. [\[CrossRef\]](#)
- Wang, R.; Li, W. Characterization models for thermal shock resistance and fracture strength of ultra-high temperature ceramics at high temperatures. *Theor. Appl. Fract. Mec.* **2017**, *90*, 1–13. [\[CrossRef\]](#)
- Zhang, Z.; Wei, C.; Liu, R.; Wu, Y.; Li, D.; Ma, X.; Liu, L.; Wang, P.; Wang, Y. Experiment and simulation analysis on thermal shock resistance of laminated ceramics with graphite and boron nitride interfaces. *Ceram. Int.* **2021**, *47*, 11973–11978. [\[CrossRef\]](#)
- Liu, H.; Wang, B.; He, Y.; Wang, C.; Song, G.; Wu, Y.; Wang, Z. Significantly enhanced thermal shock resistance of α - Si_3N_4 /O'-Sialon composite coating toughened by two-dimensional h-BN nanosheets on porous Si_3N_4 ceramics. *Ceram. Int.* **2022**, *48*, 30510–30516. [\[CrossRef\]](#)
- Tong, Y.; Zhang, H.; Hu, Y.; Zhang, P.; Hua, M.; Liang, X.; Chen, Y.; Zhang, Z. RMI-C/C-SiC-ZrSi₂ composite serving in inert atmosphere up to 2100 °C: Thermal shock resistance, microstructure and damage mechanism. *Ceram. Int.* **2021**, *47*, 20371–20378. [\[CrossRef\]](#)
- Xu, Q.; Xie, S.; Chen, Y.; Wang, Q. Thermal shock resistance and crack growth behavior of Aurivillius phase $\text{Bi}_4\text{Ti}_3\text{O}_{12}$ -based ferroelectric ceramics. *Prog. Nat. Sci. Mater.* **2021**, *31*, 248–254. [\[CrossRef\]](#)
- Nisar, A.; Bajpai, S.; Khan, M.M.; Balani, K. Wear damage tolerance and high temperature oxidation behavior of HfB_2 : ZrB_2 -SiC composites. *Ceram. Int.* **2020**, *46*, 21689–21698. [\[CrossRef\]](#)
- Daghigh, V.; Lacy, T.E.; Daghigh, H.; Gu, G.; Baghaei, K.T.; Horstemeyer, M.F.; Pittman, C.U. Machine learning predictions on fracture toughness of multiscale bio-nano-composites. *J. Reinf. Plast. Comp.* **2020**, *39*, 587–598. [\[CrossRef\]](#)
- Konstantopoulos, G.; Koumoulos, E.P.; Charitidis, C.A. Classification of mechanism of reinforcement in the fiber-matrix interface: Application of machine learning on nanoindentation data. *Mater. Des.* **2020**, *192*, 108705. [\[CrossRef\]](#)
- Laban, O.; Gowid, S.; Mahdi, E.; Musharavati, F. Experimental investigation and artificial intelligence-based modeling of the residual impact damage effect on the crashworthiness of braided Carbon/Kevlar tubes. *Compos. Struct.* **2020**, *243*, 112247. [\[CrossRef\]](#)
- Artero-Guerrero, J.A.; Pernas-Sánchez, J.; Martín-Montal, J.; Varas, D.; López-Puente, J. The influence of laminate stacking sequence on ballistic limit using a combined Experimental/FEM/Artificial Neural Networks (ANN) methodology. *Compos. Struct.* **2018**, *183*, 299–308. [\[CrossRef\]](#)

19. Yan, S.; Zou, X.; Ilkhani, M.; Jones, A. An efficient multiscale surrogate modelling framework for composite materials considering progressive damage based on artificial neural networks. *Compos. Part B* **2020**, *194*, 108014. [[CrossRef](#)]
20. LeCun, Y.; Bengio, Y.; Hinton, G. Deep learning. *Nature* **2015**, *521*, 436–444. [[CrossRef](#)]
21. Alipour, M.; Harris, D.K. Increasing the robustness of material-specific deep learning models for crack detection across different materials. *Eng. Struct.* **2020**, *206*, 110157. [[CrossRef](#)]
22. Yang, Z.; Yu, C.H.; Buehler, M.J. Deep learning model to predict complex stress and strain fields in hierarchical composites. *Sci. Adv.* **2021**, *7*, eabd7416. [[CrossRef](#)] [[PubMed](#)]
23. Mao, J.; Jain, A.K. Artificial neural networks for feature extraction and multivariate data projection. *IEEE Trans. Neural Netw.* **1995**, *6*, 296–317.
24. Yu, C.H.; Qin, Z.; Buehler, M.J. Artificial intelligence design algorithm for nanocomposites optimized for shear crack resistance. *Nano. Futures.* **2019**, *3*, 035001. [[CrossRef](#)]
25. Roberto, G.F.; Lumini, A.; Neves, L.A.; Nascimento, M.Z. Fractal Neural Network: A new ensemble of fractal geometry convolutional neural network for the classification of history images. *Expert Syst. Appl.* **2021**, *166*, 114103. [[CrossRef](#)]
26. Meng, S.; Qi, F.; Chen, H.; Wang, Z.; Bai, G. The repeated thermal shock behaviors of a ZrB₂-SiC composite heated by electric resistance method. *Int. J. Refract. Met. Hard Mater.* **2011**, *29*, 44–48. [[CrossRef](#)]
27. So, G.B.; So, H.R.; Jin, G.G. Enhancement of the box-counting algorithm for fractal dimension estimation. *Pattern Recogn. Lett.* **2017**, *98*, 53–58. [[CrossRef](#)]
28. Ivanovici, M.; Richard, N. Fractal dimension of color fractal images. *IEEE Trans. Image Process.* **2011**, *20*, 227–235. [[CrossRef](#)]
29. Zhua, J.; Hong, R.; Zhang, H.; Gu, R.; Wang, H.; Sun, F. Fired bullet signature correlation using the finite ridgelet transform (FRIT) and the gray level co-occurrence matrix (GLCM) methods. *Forensic Sci. Int.* **2022**, *330*, 111089. [[CrossRef](#)]
30. He, K.; Zhang, X.; Ren, S.; Sun, J. Deep residual learning for image recognition. *IEEE Conf. Comput. Vis. Pattern Recognit.* **2016**, 770–778.
31. Ren, S.; He, K.; Girshick, R.; Sun, J. Faster R-CNN: Towards real-time object detection with region proposal networks. *IEEE Trans. Pattern Anal. Mach. Intell.* **2017**, *39*, 1137–1149. [[CrossRef](#)] [[PubMed](#)]
32. Sun, T.; Ding, S.; Guo, L. Low-degree term first in ResNet, its variants and the whole neural network family. *Neural Netw.* **2022**, *148*, 155–165. [[CrossRef](#)] [[PubMed](#)]